Propulsion and maneuvering of an artificial microswimmer by two closely spaced waving elastic filaments

Roei Elfasi and Yossef Elimelech
Autonomous Systems and Robotics Department, Technion–Israel Institute of Technology, Haifa 3200003, Israel

Amir D. Gat
Faculty of Mechanical Engineering, Technion–Israel Institute of Technology, Haifa 3200003, Israel and Autonomous Systems and Robotics Department, Technion–Israel Institute of Technology, Haifa 3200003, Israel

(Received 23 August 2017; published 30 April 2018)

This work examines the effect of hydrodynamic interaction between two closely spaced waving elastic filaments on the propulsion and maneuvering of an artificial microswimmer. The filaments are actuated by a forced oscillation of the slope at their clamped end and are free at the opposite end. We obtain an expression for the interaction force and apply an asymptotic expansion based on a small parameter representing the ratio between the elastic deflections and the distance between the filaments. The leading-order interaction forces yield asymmetric oscillation patterns at the two frequencies (ω_1,ω_2) in which the filaments are actuated. Higher orders oscillate at frequencies which are combinations of the actuation frequencies, where the first order includes the $2\omega_1$, $2\omega_2$, $\omega_1+\omega_2$, and $\omega_1-\omega_2$ harmonics. For configurations with $\omega_1 \approx \omega_2$, the $\omega_1-\omega_2$ mode represents the dominant first-order interaction effect due to significantly smaller effective Sperm number. For in-phase actuation with $\omega_1=\omega_2$, the deflection dynamics are identical to an isolated filament with a modified Sperm number. Phase difference between the filaments is shown to have significant effect on the time-averaged forces. Optimal Sperm numbers for in-phase and antiphase actuation are calculated. Turning moments due to phase difference between the filaments are presented, yielding optimal maneuvering for phase of 90°. Calculation of the effect of hydrodynamic interaction on the propulsive forces yielded that antiphase beating is more efficient than the in-phase scenario, in contrast with the commonly used assumption of maximal efficiency of the synchronized state. Experiments are conducted to verify and illustrate some of the theoretical predictions.

DOI: 10.1103/PhysRevFluids.3.044203

I. INTRODUCTION

We study the interaction between two closely spaced oscillating elastic filaments which are immersed within a viscous liquid. The filaments are actuated by a forced oscillation of the slope at their clamped ends, which may vary in frequency, amplitude, and phase. We focus on configurations with negligible inertial effects and linear elasticity, where the dynamics are governed by a balance between viscous and elastic forces.

Various previous works examined the viscous-elastic dynamics of a single elastic filament actuated by a forced oscillation at its clamped end. These include Machin [1], who was the first to analytically obtain the deflection modes of such a passive elastic filament for the case of actuation of the slope at the fixed end. Using a similar approach, Wiggins and Goldstein [2] and Wiggins *et al.* [3] studied deflection modes and propulsion forces for forced oscillations and impulses of the position of the fixed

end, combined with a requirement of zero torque. An experimental study was conducted by Tony *et al.* [4], who measured both deflection and propulsion for a single elastic filament actuated by oscillation of the slope. The experimental data showed good agreement with both linear and nonlinear theoretical predictions. Other relevant works include Camalet and Jülicher [5], who studied the dynamics of an elastic filament actuated by internal moments, and Arco *et al.* [6], who experimentally studied oscillating flexible sheet as a novel pumping mechanism in the creeping flow regime.

Previous studies on interaction between two oscillating elastic filaments focused mainly on forced deformations in the context of synchronization dynamics between closely spaced waving flagella [7,8]. The first evidence of such synchronization was presented by Gray [9], who observed synchronized in-phase beating of spermatozoa flagella. One of the first theoretical works on synchronization of flagella was conduced by Taylor [10], who studied the simplified model of two infinite sheets with prescribed waveforms and showed that energy dissipation is minimized for in-phase oscillations and gradually increases with phase-difference. Fauci [11] compared these results with numerical simulations and showed that the phase difference evolves until sheets are either perfectly in-phase or antiphase. These observations raised a question regarding the phase locking of two nearby swimmers, since analytical and numerical studies [10–14] depicted a possible stable antiphase beating with maximum energy dissipation in contrast to biological studies [15–17] that depicted almost exclusively in-phase beating with minimal energy dissipation. A later work by Elfring and Lauga [13] showed that in configurations involving elasticity the phase difference will evolve into an in-phase beating. Other works focused on experiments in biological systems, including Brumley *et al.* [15], who demonstrated that synchronization dynamics of the *Volvox carteri* may indeed occur due to the hydrodynamic effects alone. Yang *et al.* [18] used multiparticle collision dynamics simulation technique to model the flow field around two nearby sperm cells and found that synchronization occurs when two sperm cells adjust their relative position. Once synchronization develops, the sperm cells hydrodynamically attract each other. Recent works by Goldstein *et al.* [19] and Man *et al.* [20] applied asymptotics, utilizing the distance between the filaments as a small parameter, in order to obtain analytic approximation of the interaction forces and synchronization dynamics of two oscillating filaments.

The current work aims to apply simplified experiments and linearized models (such as presented in Refs. [19] and [20]) to examine the effect of hydrodynamic interactions on the deflection patterns, forces, and moments created by an artificial microswimmer propelled by two actuated passive filaments. Of specific interest are actuations yielding to optimal propulsion energetic efficiency and effective maneuvering. This work is arranged as follows: In Sec. II we present the problem formulation, compute the interaction forces and apply asymptotic expansions. In Sec. III we present the amplitude and phase of the deflection modes and compute the the forces and moments applied by the beating filaments. In Sec. IV we define the experimental methodology and compare the experimental data to the analytic results. In Sec. V we give concluding remarks.

II. ANALYSIS

We examine the fluidic interaction between two closely spaced slender elastic filaments immersed in a viscous liquid and actuated due to a forced oscillation of the slope at their clamped end. The coordinates and configuration are illustrated in Fig. 1. The Cartesian coordinate system is denoted by (x,y,z), and time is denoted by t. The filaments, at rest, are parallel to the x direction, and their centers oscillate within the x-y plane. The fluid viscosity and density are denoted by μ and ρ, respectively. The filament flexural rigidity is s, the beam mass per-unit length is m, the gap between the centers of the filaments is d, and the gap at rest is d_0. The radius and length of the filaments are r_c and l, respectively. The forced oscillations of the slope of the filaments at $x = 0$ are at frequencies ω_i and amplitudes ϕ_i (where $i = 1$ and $i = 2$ denote filaments 1 and 2, respectively). The phase difference between the forced oscillations is γ. The deflection of the filaments is v_i, where we define an auxiliary average deflection $v_a = (v_1 + v_2)/2$ and an auxiliary relative deflection $v_d = (v_1 - v_2)/2$. The perpendicular drag coefficient of the filaments is $\xi_\perp$.

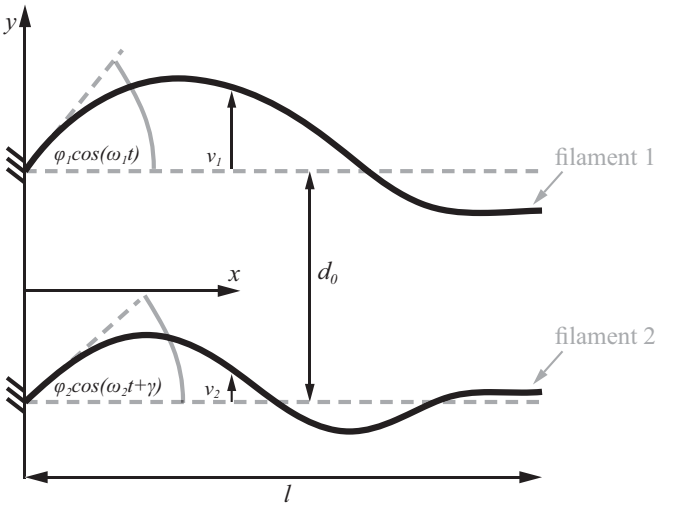

FIG. 1. Illustration of the examined configuration consisting of two oscillating elastic filaments immersed in a viscous fluid. The filaments, at rest, are parallel to the x axis, and their centers oscillate within the x-y plane. The distance between the bases of the filaments is d_0, and the deflections are denoted by v_1 and v_2 for filament 1 and 2, respectively. The length of both filaments is l.

Hereafter, asterisk superscripts denote characteristic values and capital letters denote normalized variables. The characteristic average deflection is v_a^*, characteristic relative deflection is v_d^* and characteristic frequency is ω^*. We define the small parameters [where $v^* = \max(v_a^*, v_d^*)$]:

$$\frac{\rho\omega^*(v^*)^2}{\mu} \ll 1, \quad \frac{m(\omega^* v^*)^2}{s} \ll 1, \quad \frac{d_0}{l} \ll 1,$$
$$\frac{r_c}{d_0} \ll 1, \quad \frac{v_a^*}{l} \ll 1, \quad \varepsilon = \frac{v_d^*}{d_0} \ll 1, \tag{1}$$

corresponding to assumptions of negligible fluidic inertia (small Womersley number), negligible solid inertia, small gap to filament length ratio, small filament radius to gap ratio, small average deflection to length ratio, and small relative deflection to gap ratio.

In addition, we apply the commonly used approximation [see Refs. 1–4,21–24] of perpendicular viscous drag of the form $\Delta w \xi_\perp$, where Δw is the relative perpendicular speed between the filament and the surrounding fluid and the coefficient $\xi_\perp$ is approximately constant throughout the filament. We define the function $\Lambda(d)$ as the ratio of the induced fluid speed due to the adjacent filament and the velocity of the adjacent filament. Thus, under the above assumptions, the deflection of the filaments is governed by

$$s\frac{\partial^4 v_i}{\partial x^4} = -\xi_\perp\left[\frac{\partial v_i}{\partial t} - \Lambda(d)\frac{\partial v_j}{\partial t}\right], \tag{2a}$$

where $d = d_0 + v_1 - v_2$, supplemented by the boundary conditions

$$\frac{\partial v_i(0,t)}{\partial x} = \phi_i e^{i2\pi[\omega_i t + (i-1)\gamma]},$$
$$v_i(0,t) = \frac{\partial^2 v_i(l,t)}{\partial x^2} = \frac{\partial^3 v_i(l,t)}{\partial x^3} = 0, \tag{2b}$$

where for filament 1, $(i,j) = (1,2)$ and for filament 2, $(i,j) = (2,1)$.

The flow field due to a slender filament moving relative to a viscous fluid in the creeping flow regime may be approximated by a uniform distribution of Stokeslets and dipoles positioned along the centerline of the filament. For motion perpendicular to the centerline, the magnitude of the Stokeslet distribution is $\xi_\perp \Delta w$, and the dipole magnitude is $r_c^2 \xi_\perp \Delta v/4\mu$, where $\xi_\perp \approx 8\pi\mu/[0.386 + \ln(l^2/r_c^2)]$ [22]. Thus, the induced speed may be approximated by (using the same integral approximations and approach used in Ref. [22])

$$\Lambda(d) \approx \frac{\xi_\perp}{4\pi\mu}\left[1 + \ln\left(\frac{2l}{d}\right)\right]. \tag{3}$$

[See the derivation of Eq. (14) in Ref. [20], which is identical in leading order.]

Equations (2) may be decoupled by subtracting the equation governing filament 2 from the equation governing filament 1, and substituting relative deflection $v_d = (v_1 - v_2)/2$, thus isolating v_d. Similarly, by addition of the governing equations of both filaments and substituting average deflection $v_a = (v_1 + v_2)/2$, the governing equation for v_a may be obtained, which, however, does depends on v_d.

We define the normalized axial coordinate $X = x/l$, normalized time $T = t2\pi\omega^*$, normalized average deflection $V_d = v_d/v_d^*$, normalized relative deflection $V_a = v_a/v_a^*$, normalized angular speeds $(\Omega_1, \Omega_2) = (\omega_1/\omega^*, \omega_2/\omega^*)$, and normalized gap $D = d/d_0 = 1 + v_1/d_0 - v_2/d_0$.

Substituting normalized variables, the equations governing V_a and V_d are

$$\frac{\partial^4 V_d}{\partial X^4} = -S_p^4[1 + \Lambda(D = 1 + 2\varepsilon V_d)]\frac{\partial V_d}{\partial T} \tag{4a}$$

and

$$\frac{\partial^4 V_a}{\partial X^4} = -S_p^4[1 - \Lambda(D = 1 + 2\varepsilon V_d)]\frac{\partial V_a}{\partial T}, \tag{4b}$$

where $S_p = (\xi_\perp l^4 2\pi\omega^*/s)^{1/4}$ is the Sperm number. Equations (4) are supplemented by the normalized boundary conditions

$$V_d\big|_{X=0} = 0, \quad \frac{\partial V_d}{\partial X}\Big|_{X=0} = \frac{\phi_1 l}{2v_d^*}e^{i\Omega_1 T} - \frac{\phi_2 l}{2v_d^*}e^{i(\Omega_2 T + 2\pi\gamma)}, \tag{5a}$$

$$V_a\big|_{X=0} = 0, \quad \frac{\partial V_a}{\partial X}\Big|_{X=0} = \frac{\phi_1 l}{2v_a^*}e^{i\Omega_1 T} + \frac{\phi_2 l}{2v_a^*}e^{i(\Omega_2 T + 2\pi\gamma)}, \tag{5b}$$

representing the hinge boundary condition and slope actuation at $X = 0$ and

$$\frac{\partial^2 V_d}{\partial X^2}\Big|_{X=1} = \frac{\partial^3 V_d}{\partial X^3}\Big|_{X=1} = 0, \tag{5c}$$

$$\frac{\partial^2 V_a}{\partial X^2}\Big|_{X=1} = \frac{\partial^3 V_a}{\partial X^3}\Big|_{X=1} = 0, \tag{5d}$$

representing the free end at $X = 1$. From (5), the characteristic values v_a^* and v_d^* may be defined as

$$v_d^* = \max\left[\frac{\phi_1 l}{2}\cos(\Omega_1 T) - \frac{\phi_2 l}{2}\cos(\Omega_2 T + 2\pi\gamma)\right] \tag{6a}$$

and

$$v_a^* = \max\left[\frac{\phi_1 l}{2}\cos(\Omega_1 T) + \frac{\phi_2 l}{2}\cos(\Omega_2 T + 2\pi\gamma)\right]. \tag{6b}$$

Applying the linearization scheme presented in Ref. [20], asymptotic expansion of the nonlinear (4) allows for approximation to a set of linear equations at the limit $\varepsilon = v_d^*/d_0 \ll 1$, by presenting $\Lambda(D)$ as a Taylor series around $D = 1$:

$$\Lambda(D) \sim \Lambda(1) + \varepsilon 2V_d \frac{\partial \Lambda(D)}{\partial D} + \frac{(2\varepsilon V_d)^2}{2} \frac{\partial^2 \Lambda(D)}{\partial D^2}, \tag{7}$$

as well as asymptotically expanding V_d and V_a:

$$V_d \sim V_{d,0} + \varepsilon V_{d,1} + \varepsilon^2 V_{d,2}, \quad V_a \sim V_{a,0} + \varepsilon V_{a,1} + \varepsilon^2 V_{a,2}. \tag{8}$$

Substituting (7) and (8) into (4) and defining the differential operators $L^+ = \partial^4/\partial X^4 + S_p^4[1 + \Lambda(1)]\partial/\partial T$ and $L^- = \partial^4/\partial X^4 + S_p^4[1 - \Lambda(1)]\partial/\partial T$ yields the leading order $O(1)$ of (4):

$$L^+ V_{d,0} = 0, \quad L^- V_{a,0} = 0, \tag{9}$$

as well as order $O(\varepsilon)$,

$$L^+ V_{d,1} = -2S_p^4 V_{d,0} \frac{\partial V_{d,0}}{\partial T} \frac{\partial \Lambda(D)}{\partial D}, \quad L^- V_{a,1} = 2S_p^4 V_{d,0} \frac{\partial V_{a,0}}{\partial T} \frac{\partial \Lambda(D)}{\partial D}, \tag{10}$$

and order $O(\varepsilon^2)$,

$$\begin{aligned} L^+ V_{d,2} &= -2S_p^4 \left\{ \frac{\partial V_{d,0}}{\partial T} \left[V_{d,1} \frac{\partial \Lambda(D)}{\partial D} + V_{d,0}^2 \frac{\partial^2 \Lambda(D)}{\partial D^2} \right] + \frac{\partial V_{d,1}}{\partial T} V_{d,0} \frac{\partial \Lambda(D)}{\partial D} \right\}, \\ L^- V_{a,2} &= 2S_p^4 \left\{ \frac{\partial V_{a,0}}{\partial T} \left[V_{d,1} \frac{\partial \Lambda(D)}{\partial D} + V_{d,0}^2 \frac{\partial^2 \Lambda(D)}{\partial D^2} \right] + \frac{\partial V_{a,1}}{\partial T} V_{d,0} \frac{\partial \Lambda(D)}{\partial D} \right\}, \end{aligned} \tag{11}$$

and so forth. The boundary conditions for the $O(1)$ (9) are identical to (5). For the $O(\varepsilon)$ (10) and $O(\varepsilon^2)$ (11) equations, the boundary conditions (5) are modified so that $\partial V_{d,1}/\partial X = \partial V_{a,1}/\partial X = \partial V_{d,2}/\partial X = \partial V_{a,2}/\partial X = 0$ at $X = 0$.

The leading-order $V_{d,0}$ solution can be presented by

$$\begin{aligned} V_{d,0} &= \mathbb{R}\mathrm{e}[e^{i\Omega_1 T} G_{\Omega_1,d}(X) - e^{i(\Omega_2 T + 2\pi\gamma)} G_{\Omega_2,d}(X)] \\ &= \tfrac{1}{2}\{|G_{\Omega_1,d}(X)|[e^{i\{\Omega_1 T + \arg[G_{\Omega_1,d}(X)]\}} + e^{-i\{\Omega_1 T + \arg[G_{\Omega_1,d}(X)]\}}] \\ &\quad - |G_{\Omega_2,d}(X)|[e^{i\{\Omega_2 T + 2\pi\gamma + \arg[G_{\Omega_2,d}(X)]\}} + e^{-i\{\Omega_2 T + 2\pi\gamma + \arg[G_{\Omega_2,d}(X)]\}}]\}, \end{aligned} \tag{12}$$

where the functions $G_{\Omega_1,d}(X)$, $G_{\Omega_2,d}(X)$ are

$$\begin{aligned} G_{\Omega_1,d}(X) = \frac{\phi_1 l}{2v_d^*} \frac{e^{i\frac{\pi}{8}}\{S_p \sqrt[4]{\Omega_1[1 + \Lambda(1)]}\}^{-1}}{\left(2 + 2\cos\phi_d^1 \cosh\phi_d^1\right)} \big[&\sin\theta_d^1 + \sinh\theta_d^1 + \sin\phi_d^1 \cosh\left(\phi_d^1 - \theta_d^1\right) \\ &- \cos\phi_d^1 \sinh\left(\phi_d^1 - \theta_d^1\right) - \cosh\phi_d^1 \sin\left(\phi_d^1 - \theta_d^1\right) + \sinh\phi_d^1 \cos\left(\phi_d^1 - \theta_d^1\right)\big] \end{aligned} \tag{13}$$

and

$$\begin{aligned} G_{\Omega_2,d}(X) = \frac{\phi_2 l}{2v_d^*} \frac{e^{i\frac{\pi}{8}}\{S_p \sqrt[4]{\Omega_2[1 + \Lambda(1)]}\}^{-1}}{\left(2 + 2\cos\phi_d^2 \cosh\phi_d^2\right)} \big[&\sin\theta_d^2 + \sinh\theta_d^2 + \sin\phi_d^2 \cosh\left(\phi_d^2 - \theta_d^2\right) \\ &- \cos\phi_d^2 \sinh\left(\phi_d^2 - \theta_d^2\right) - \cosh\phi_d^2 \sin\left(\phi_d^2 - \theta_d^2\right) + \sinh\phi_d^2 \cos\left(\phi_d^2 - \theta_d^2\right)\big], \end{aligned} \tag{14}$$

and where $\theta_d^i = X S_p \sqrt[4]{\Omega_i[1 + \Lambda(1)]} e^{-i\pi/8}$, $\phi_d^i = S_p \sqrt[4]{\Omega_i[1 + \Lambda(1)]} e^{-i\pi/8}$. Applying the relevant homogeneous boundary conditions and substituting (14) into (10), we obtain that $V_{d,1}$ is of the form

$$\begin{aligned} V_{d,1} = \mathbb{R}\mathrm{e}[&G_{2\Omega_1,d}(X) e^{i2\Omega_1 T} + G_{2\Omega_2,d}(X) e^{i2\Omega_2 T} \\ &+ G_{(\Omega_1+\Omega_2),d}(X) e^{i(\Omega_1+\Omega_2)T} + G_{(\Omega_1-\Omega_2),d}(X) e^{i(\Omega_1-\Omega_2)T}], \end{aligned} \tag{15}$$

where the functions $G_{2\Omega_1,d}(X)$, $G_{2\Omega_2,d}(X)$, $G_{(\Omega_1+\Omega_2),d}(X)$, and $G_{(\Omega_1-2\Omega_2),d}(X)$ may be readily obtained by substituting (12) into (10), isolating each harmonic and solving the corresponding ordinary differential equation. Substituting (15) and (12) into (11) yields $V_{d,2}$ with the harmonics Ω_1, $3\Omega_1$, Ω_2, $3\Omega_2$, $2\Omega_1+\Omega_2$, $\Omega_1+2\Omega_2$, $2\Omega_1-\Omega_2$, and $2\Omega_1-\Omega_2$. The corresponding functions $V_{a,0}$, $V_{a,1}$, and $V_{a,2}$ can be calculated by applying a similar approach and will have identical frequencies, but different mode functions, compared to $V_{d,0}$, $V_{d,1}$, and $V_{d,2}$:

$$\begin{aligned} V_{a,0} &= \mathbb{R}\mathrm{e}[e^{i\Omega_1 T}G_{\Omega_1,a}(X) + e^{i(\Omega_2 T+2\pi\gamma)}G_{\Omega_2,a}(X)] \\ &= \tfrac{1}{2}\{|G_{\Omega_1,a}(X)|[e^{i\{\Omega_1 T+\arg[G_{\Omega_1,a}(X)]\}} + e^{-i\{\Omega_1 T+\arg[G_{\Omega_1,a}(X)]\}}] \\ &\quad + |G_{\Omega_2,a}(X)|[e^{i\{\Omega_2 T+2\pi\gamma+\arg[G_{\Omega_2,a}(X)]\}} + e^{-i\{\Omega_2 T+2\pi\gamma+\arg[G_{\Omega_2,a}(X)]\}}]\}, \end{aligned} \tag{16}$$

$$\begin{aligned} G_{\Omega_1,a}(X) = \frac{\phi_1 l}{2v_a^*}\frac{e^{i\frac{\pi}{8}}\{S_p\sqrt[4]{\Omega_1[1-\Lambda(1)]}\}^{-1}}{\left(2+2\cos\phi_a^1\cosh\phi_a^1\right)}\big[&\sin\theta_a^1+\sinh\theta_a^1+\sin\phi_a^1\cosh\left(\phi_a^1-\theta_a^1\right) \\ &-\cos\phi_a^1\sinh\left(\phi_a^1-\theta_a^1\right)-\cosh\phi_a^1\sin\left(\phi_a^1-\theta_a^1\right)+\sinh\phi_a^1\cos\left(\phi_a^1-\theta_a^1\right)\big], \end{aligned} \tag{17}$$

$$\begin{aligned} G_{\Omega_2,a}(X) = \frac{\phi_2 l}{2v_a^*}\frac{e^{i\frac{\pi}{8}}\{S_p\sqrt[4]{\Omega_2[1-\Lambda(1)]}\}^{-1}}{\left(2+2\cos\phi_a^2\cosh\phi_a^2\right)}\big[&\sin\theta_a^2+\sinh\theta_a^2+\sin\phi_a^2\cosh\left(\phi_a^2-\theta_a^2\right) \\ &-\cos\phi_a^2\sinh\left(\phi_a^2-\theta_a^2\right)-\cosh\phi_a^2\sin\left(\phi_a^2-\theta_a^2\right)+\sinh\phi_a^2\cos\left(\phi_a^2-\theta_a^2\right)\big], \end{aligned} \tag{18}$$

and where $\theta_a^i = XS_p\sqrt[4]{\Omega_i[1-\Lambda(1)]}e^{-i\pi/8}$, $\phi_a^i = S_p\sqrt[4]{\Omega_i[1-\Lambda(1)]}e^{-i\pi/8}$.

In Eqs. (12)–(15), describing the average deflection of both filaments $V_d = (V_1+V_2)/2$, the Sperm number is multiplied everywhere by $S_p\sqrt[4]{\Omega_i[1+\Lambda(1)]}$. A different modified Sperm number $S_p\sqrt[4]{\Omega_i[1-\Lambda(1)]}$ appears in Eqs. (16)–(18) describing the difference between the deflections of both filaments $V_a = (V_1-V_2)/2$. Since $V_a = 0$ for in-phase actuation and $V_d = 0$ for antiphase actuation, $S_p\sqrt[4]{\Omega_i[1+\Lambda(1)]}$ and $S_p\sqrt[4]{\Omega_i[1-\Lambda(1)]}$ can be viewed as in-phase and antiphase modified Sperm numbers.

III. RESULTS

Figure 2 presents the amplitude and phase of the harmonics comprising V_1 versus the coordinate X, for various configurations where $\varepsilon = 0.1$ and $S_p = 2.1$. In all cases the filaments are actuated at amplitudes $\phi_1 = \phi_2 = 15^\circ$ and the normalized frequency of filament 1 is $\Omega_1 = 0.5$. Panels (a)–(d) present the effect of phase difference γ for filaments actuated at identical frequencies $\Omega_2 = \Omega_1$. For comparison, an isolated filament is presented by a gray smooth line. The interaction with an adjacent filament with $\gamma = 0$ decreases the effective Sperm number, thus increasing the effective stiffness of the filament and amplitude $|F_\Omega|$. This occurs since hydrodynamic interaction with a second filament oscillating without phase reduces the viscous force on the filament, thus modifying the viscous-elastic oscillation dynamics. This yields deflection dynamics identical to an isolated filament with a modified Sperm number $S_p[1-\Lambda(1)]^{1/4}$, where $\Lambda(1)$ is the leading-order interaction term. Similarly, the leading-order effect of an adjacent filament oscillating at antiphase $\gamma = \pi$ is to increase the effective Sperm number to $S_p[1+\Lambda(1)]^{1/4}$, thus decreasing the deflection of the filament. For $\gamma = 0$ the first-order is identically zero, while for both $\gamma = \pi/2$ and $\gamma = \pi$ (see panels c and d) the phase of the first-order correction is nearly independent of X and with values under $\approx 10^\circ$. Panels (e–f) examine the effect of an adjacent oscillating filament with $\Omega_2 = 0.2\Omega_1$ and no phase $\gamma = 0$. Similarly, panels (i–l) examine the opposite case of $\Omega_2 = 5\Omega_1$ and $\gamma = 0$. The leading-order effect of the adjacent filament is significant for $\Omega_2 = 0.2\Omega_1$ (where it has a similar effect to the leading-order direct actuation of the filament; see panel e). However, a smaller effect is evident for the case $\Omega_2 = 5\Omega_1$ (see panel i). Panels (f) and (j) examine the phase of the leading-order modes, presenting an opposite effect where the phase is small and nearly uniform for $\Omega_2 = 0.2\Omega_1$ and significant for the case of $\Omega_2 = 5\Omega_1$. The first-order modes (see panels g and k) are dominated by the small frequencies,

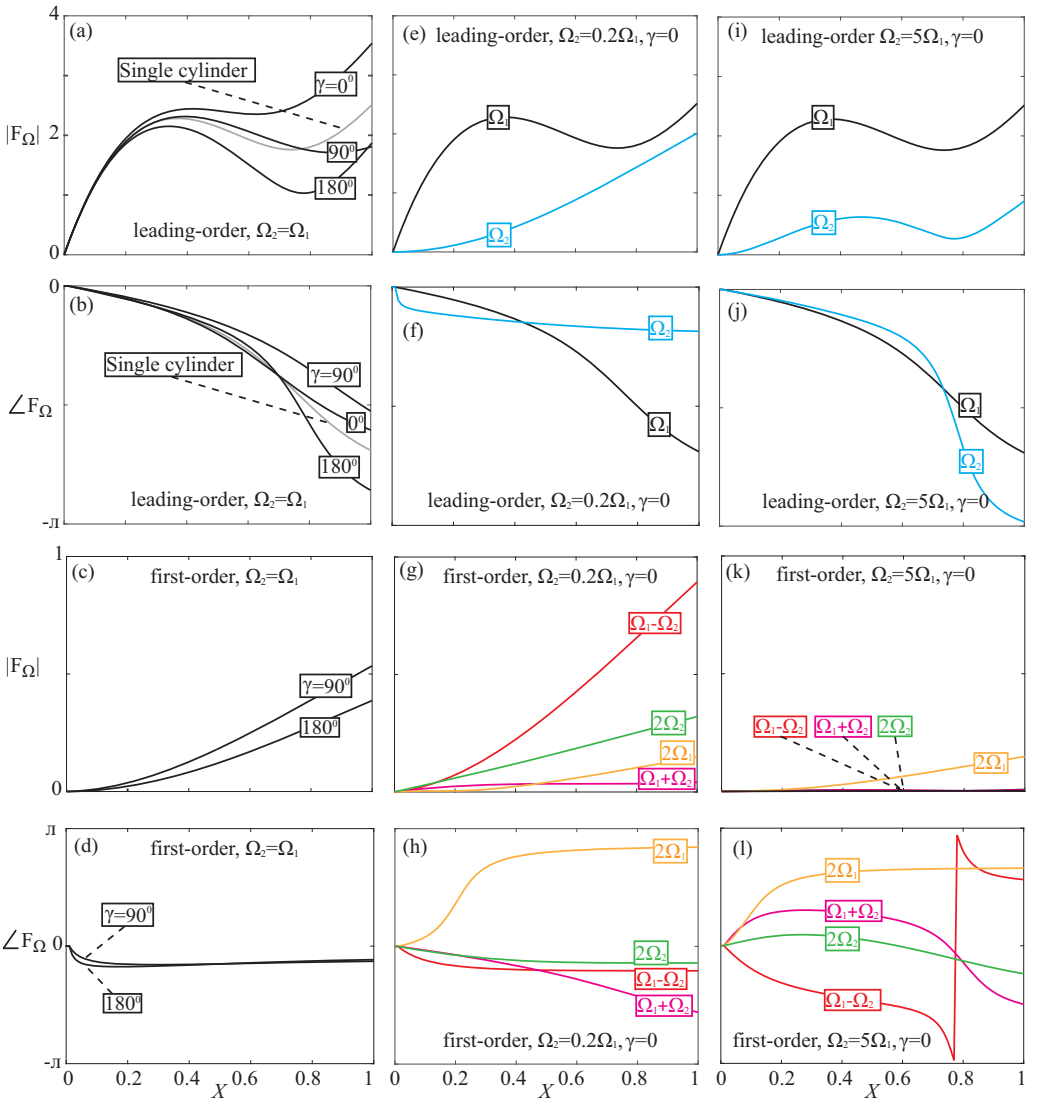

FIG. 2. Axial distributions of the amplitude and phase of the frequencies comprising v_1 for various configurations. In all cases filament 1 is actuated with amplitude $\phi_1 = 15^\circ$ and frequency $\Omega_1 = 0.5$, the amplitude of filament 2 is $\phi_2 = \phi_1$, $\varepsilon = 0.1$, and $S_p = 2.1$. Panels (a)–(d) examine the effect of phase γ difference for $\Omega_2 = \Omega_1$. The modes presented in panels (a), (b) oscillate at frequency Ω_1, and the modes presented in panels (c), (d) oscillate at frequency $2\Omega_1$. Panels (e)–(h) examine the effect of an adjacent oscillating filament with $\Omega_2 = 0.2\Omega_1$ and $\gamma = 0$. Panels (i)–(l) examine the effect of $\Omega_2 = 5\Omega_1$ and $\gamma = 0$.

corresponding to smaller effective Sperm numbers of the interaction. Thus, for configurations in which the minimal frequency (from the set $2\Omega_1, 2\Omega_2, \Omega_1 + \Omega_2, |\Omega_1 - \Omega_2|$) is significantly smaller than all other frequencies, the first-order dynamics may be reasonably approximated by the minimal frequency mode alone (see panel k).

The deflection modes calculated in Sec. III can be applied to calculate the effect of hydrodynamic interaction between the filaments on the forces and moments acting on an artificial swimmer as illustrated in Fig. 3. Assuming the viscous resistance of the swimmer body is sufficiently large, the velocity of the swimmer is negligible compared with the oscillating velocities of the filaments, and

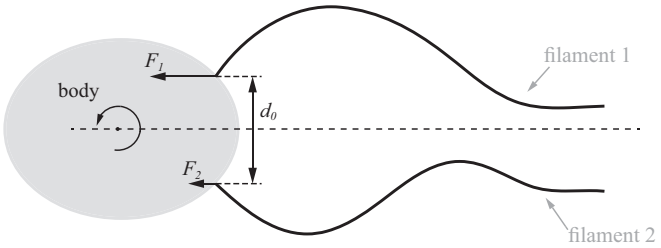

FIG. 3. Schematic description of an artificial swimmer with two waving elastic filaments actuated at the base. Turning moment may be generated by difference in the average propulsion forces of the filaments.

thus the force may be computed from [4]

$$f_i = \int_0^l s\frac{\xi_\perp - \xi_\parallel}{\xi_\perp}\frac{\partial v}{\partial x}\frac{\partial^4 v}{\partial x^4}\,dx = s\frac{\xi_\perp - \xi_\parallel}{\xi_\perp}\left[\frac{\partial v}{\partial x}\frac{\partial^3 v}{\partial x^3} - \frac{1}{2}\frac{\partial^2 v}{\partial x^2}^2\right]_{x=0}. \tag{19}$$

We define the normalized time-average force in the X direction, denoted by $\langle \mathcal{F}_i \rangle$, as

$$\langle \mathcal{F}_i \rangle = \frac{1}{T}\int_0^T \left\{\frac{\partial V_i(0,\tau)}{\partial X}\frac{\partial^3 V_i(0,\tau)}{\partial X^3} - \frac{1}{2}\left[\frac{\partial V_i(0,\tau)}{\partial X}\right]^2\right\} d\tau, \tag{20}$$

where $T \to \infty$, $l_0 = \sqrt[4]{s/(2\pi\omega\xi_\perp)}$ $X = x/l_0$, $V_i = v_i/l_0\phi^*$, $\xi_\perp = 4\pi\mu/[\ln(l/r_c) + 0.193]$, $\xi_\parallel = 2\pi\mu/[\ln(l/r_c) - 0.807]$, and $\mathcal{F}_i = f_i/(\phi^{*2}l_0^2)2\pi\omega(\xi_\perp - \xi_\parallel)$.

Similarly, for given waving parameters, the energy required to generate actuation of the filaments can be related to the moment at the clamped end of the filament by

$$\langle \mathcal{E}_i \rangle = \int_0^T \left|\frac{\partial^2 V_i(0,\tau)}{\partial X^2}\frac{\partial^2 V_i(0,\tau)}{\partial X \partial \tau}\right| d\tau, \tag{21}$$

where $\langle \mathcal{E}_i \rangle$ is scaled by $s\phi^*/l_0$. The total energy applied to propulsion of a swimmer is $\int_0^T f_i u_p\,dt = \int_0^T f_i^2\,dt/c_d$, where u_p is the speed of the swimmer and c_d is the viscous drag coefficient. In

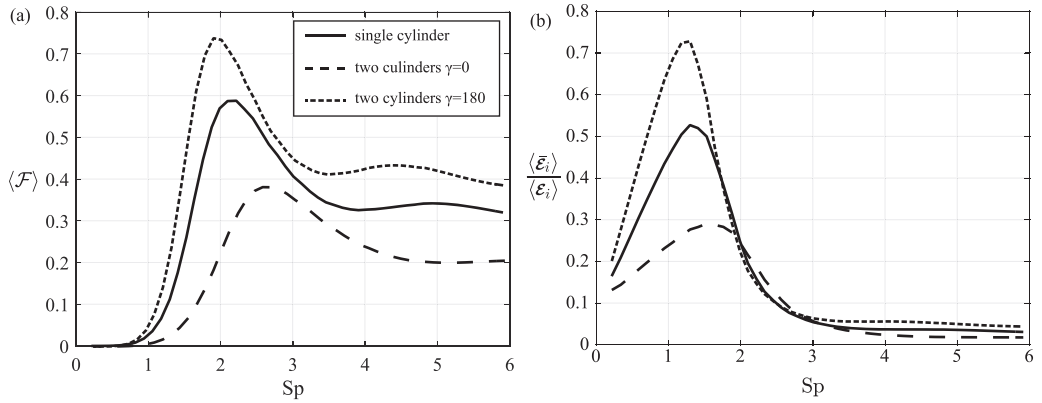

FIG. 4. Average force in the x direction (a) and the ratio $\langle \mathcal{F}_i \rangle / \langle \mathcal{M}_i \rangle$ (b), which is proportional to energetic efficiency, vs the Sperm number $S_p = l/l_0$. In all cases, $\phi_1 = \phi_2 = 25^\circ$, $l_0 = \sqrt[4]{s/(2\pi\omega\xi_\perp)} = 70\,\text{mm}$ (and $\omega_1 = \omega_2$), $d_0 = 14\,\text{mm}$, and $r_c = 0.5\,\text{mm}$. Isolated filament is marked by smooth lines. Beating filament with an adjacent filament beating in-phase in marked by dashed lines. Beating filament with an adjacent filament beating in antiphase is marked by dotted line.

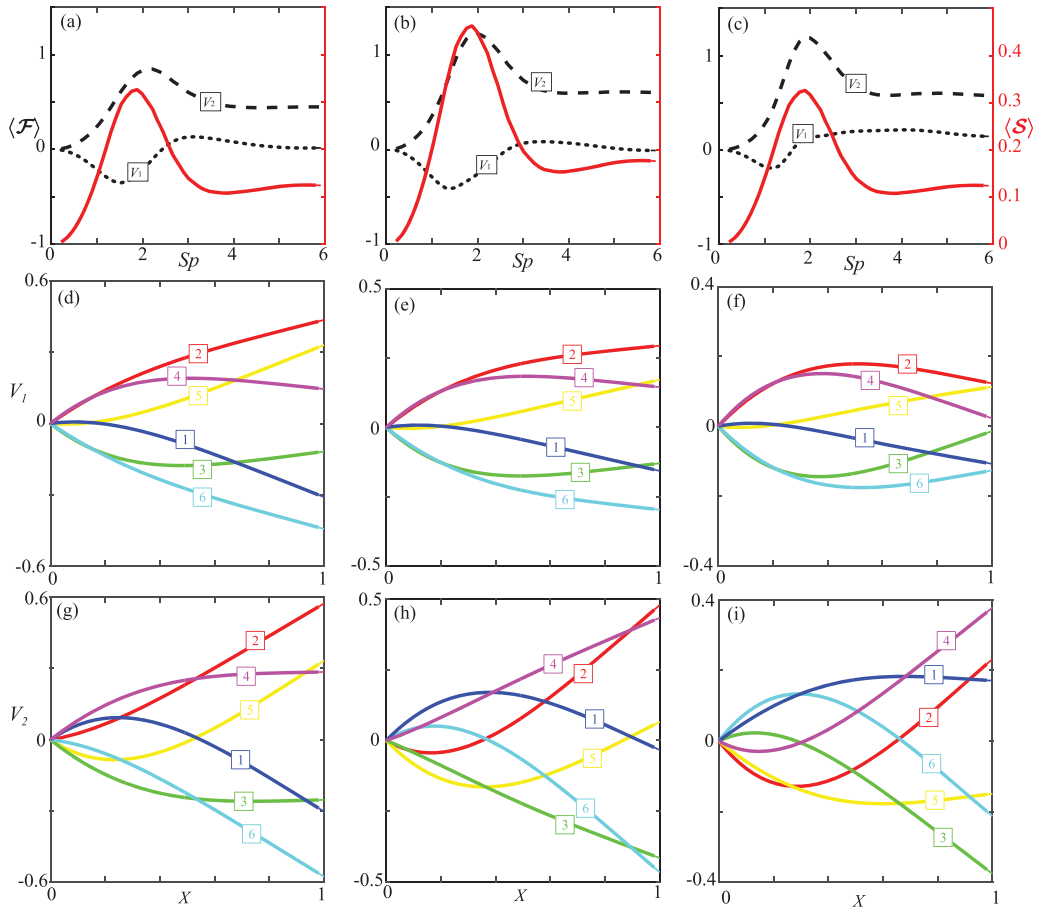

FIG. 5. Average propulsion force vs Sperm number for filaments 1 (dotted lines) and 2 (dashed lines) with phase difference of 45° (a), 90° (b), and 135° (c). The steering moment is marked by the red solid line in panels (a)–(c). Panels (d), (e), and (f) present deflection patterns of filament 1 for 45°, 90°, and 135°, respectively. Panels (g), (h), and (i) present deflection patterns for $S_p = 2.45$ of filament 2 for 45°, 90°, and 135°, respectively. The tags at panels (d)–(i) mark six equally spaced times along the full oscillation period of the first filament. With the exception of phase, all parameters are identical to Fig. 4.

normalized parameters, the total applied energy is given by

$$\langle \bar{\mathcal{E}}_i \rangle = \frac{1}{C_D} \int_0^T \left\{ \frac{\partial V_i(0,\tau)}{\partial X} \frac{\partial^3 V_i(0,\tau)}{\partial X^3} - \frac{1}{2} \left[\frac{\partial V_i(0,\tau)}{\partial X} \right]^2 \right\}^2 d\tau. \tag{22}$$

Thus, (21) and (22) allow us to estimate the energetic efficiency of the swimmer by the ratio $\langle \bar{\mathcal{E}}_i \rangle / \langle \mathcal{E}_i \rangle$.

Figure 4 presents the average propulsive force (a) and the ratio $\langle \mathcal{E}_i \rangle / \langle \bar{\mathcal{E}}_i \rangle$ (b), which is proportional to energetic efficiency, versus the Sperm number $S_p = l/l_0$. The parameter l_0 is kept constant while l varies in order to solve (4)–(6) for different Sperm numbers. In all cases both filaments are actuated at the same frequency and amplitude $\phi_1 = \phi_2 = 25°$, $l_0 = 70\,\text{mm}$, $d_0 = 14\,\text{mm}$, and $r_c = 0.5\,\text{mm}$. Results for isolated filament (smooth lines), beating filament with an adjacent filament beating in-phase ($\gamma = 0°$, dashed lines), and beating filament with an adjacent filament beating in antiphase ($\gamma = 180°$, dotted line) are presented. Previous studies [2,4], showed that the maximal propulsive force is generated for $S_p \approx 2.1$. However, when a second beating filament is introduced to the system, the optimal Sperm number is modified. Antiphase beating reduces the optimal Sperm number,

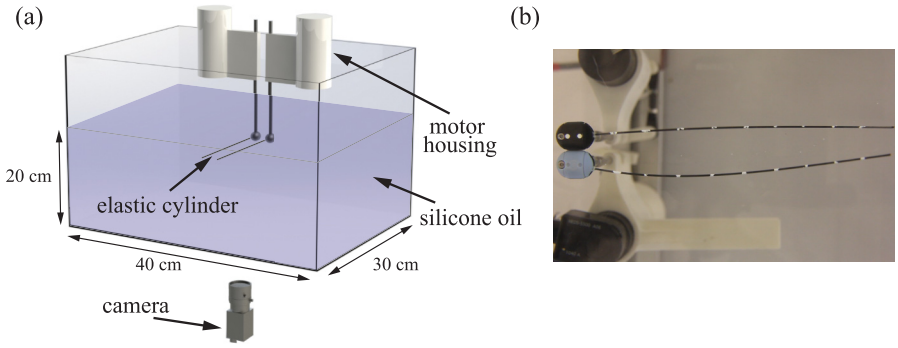

FIG. 6. (a) Schematic description of the experimental setup consisting of two elastic filaments deforming due to a prescribed oscillation of the slope at their bases. (b) An illustrative frame obtained with the Canon EOS 60D DSLR camera during an experiment.

while in-phase beating increases the optimal sperm number. The modified optimal number can be estimated from the leading-order equations by the condition $S_p = l/l_0 \approx 2.1[1 - \Lambda(l,d_0)]^{1/4}$ for in-phase beating $\gamma = 0$ and $S_p = l/l_0 \approx 2.1[1 + \Lambda(l,d_0)]^{1/4}$ for antiphase beating $\gamma = \pi$. For the physical and geometric properties examined in Fig. 4, these conditions yield optimal values of $S_p = l/l_0 \approx 2.4$ for in-phase beating and $S_p = l/l_0 \approx 1.6$ for antiphase beating. Panel (a), which includes first-order interactions with $\varepsilon = 0.1$, presents extrema of $S_p = 2.6$ for in-phase beating and $S_p = 1.9$ for antiphase beating. In addition, hydrodynamic interaction for in-phase beating decreases the propulsion force as well as the energetic efficiency (see panel b) compared with an isolated filament. In contrast, antiphase beating is shown to be an optimal actuation with regard to phase, increasing the propulsive force as well as the energetic efficiency. However, as S_p increases, the differences in energetic efficiency are reduced, and for an intermediate range of S_p the in-phase mode is preferable. For all presented configurations, the optimal energetic efficiency is at significantly lower values of S_p compared with the optimal propulsion force presented in panel (a).

Figure 5 presents the force generated for the two filaments as a function of Sperm number for cases where the phase difference is not zero. Due to the asymmetric hydrodynamic interaction, there are different average propulsive forces of filament 1 and 2, which create a turning moment acting on the body, defined as $\langle \mathcal{S} \rangle$ where

$$\langle \mathcal{S} \rangle = \frac{d_0}{2\phi^* l_0}(\langle \mathcal{F}_1 \rangle - \langle \mathcal{F}_2 \rangle). \tag{23}$$

Panels (a), (b), and (c) in Fig. 5 present the time-averaged forces for filament 1 (dotted lines) and filament 2 (dashed lines) for phases of $\gamma = 0^\circ$, 90°, and 135°, respectively. The corresponding deflection patterns of the filaments are illustrated in panels (d)–(f) for filament 1 and (g)–(i) for filament 2. In all cases in panels (d)–(i) $S_p = 2.45$. While the hydrodynamic interaction yields only a small effect on the propulsion force, it creates a significant effect on the time-averaged propulsion force and in some cases reverses the direction of the force applied by the waving filament. This occurs since, without hydrodynamic interactions, time-averaged propulsion forces are created only due to small fluid-induced elastic deflections breaking the symmetry of the waving filaments. The addition of a second waving filament creates an additional mechanism for asymmetry during the beating period. The time-average turning moment $\langle \mathcal{S} \rangle$ [see panels (a)–(c)] is marked by a red smooth line, presenting maximal turning moments for $S_p \approx 1.9$ for all of the examined phases. The case of $\gamma = 90^\circ$ generates the highest steering moment, due to increased resistance acting on filament 1, and reduced resistance on filament 2, throughout beating cycle [see panels (e) and (h)].

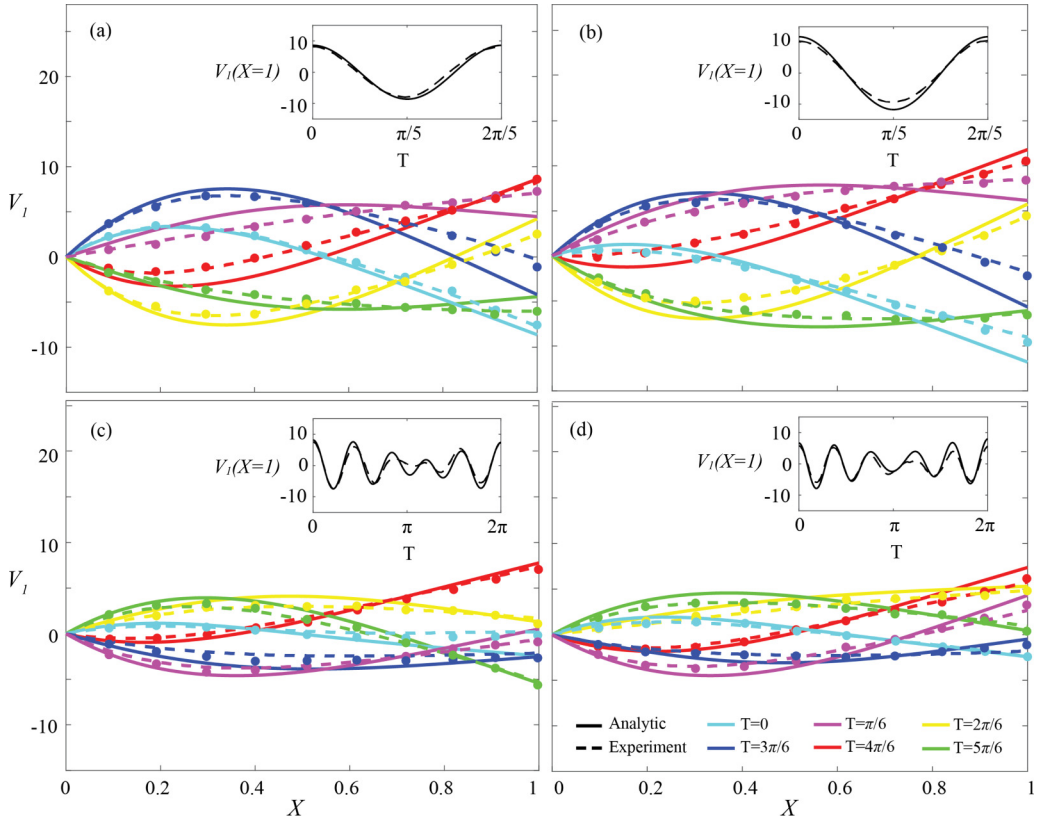

FIG. 7. Deflection V_1 of filament 1 for $\Omega_1 = 5$ and amplitude $\phi_1 = \phi_2 = 15^\circ$ at six equally spaced times along the full oscillation period P. Dimensional values are $v_1 = V_1 \times 1.4\,\text{mm}$, $\omega = \Omega \times 0.1\,\text{Hz}$, $x = X \times 150\,\text{mm}$, and $t = T \times 0.62\,\text{s}$. Smooth lines denote theoretical results, dots denote experimental data, and dashed lines denote experimental data polynomial fit. The examine cases are (a) without an adjacent filament, (b) an adjacent filament with $\Omega_1 = \Omega_2$, (c) $\Omega_2 = 0.8\Omega_1$, and (d) $\Omega_2 = 1.2\Omega_1$. Inserts present the deflection of the filament at its free end $V_1(X = 1)$ vs time. See movies 1–4 in Ref. [26].

IV. EXPERIMENTS

Experiments were conducted to quantify the interaction between the two oscillating elastic filaments and validate the results presented in Sec. II. The experimental setup is illustrated in Fig. 6. Actuation is achieved by a pair of Faulhaber 3257G024CR DC motors operating outside of the fluid, where motion is transferred to the filaments through levers connected to elongated rotation axes. The bases of the filaments are fixed while the slopes at the bases are forced to oscillate at predetermined amplitude and frequency. The motors controller is an iPOS4808 BX-CAN drive, and the elastic filaments are composed of carbon fiber with diameter of 1 mm and length of 150 mm. The gap at rest between the filaments is $d_0 = 14\,\text{mm}$. The immersing fluid is Xiameter®PMX-200 Silicone oil with viscosity $\mu = 59.2\,\text{Pa}\cdot\text{s}$ and density $\rho_l = 987\,\text{kg/m}^3$. The container dimensions are $0.4\,\text{m} \times 0.3\,\text{m} \times 0.2\,\text{m}$, and the elastic filaments are placed symmetrically to both sides of the container center plane (see Fig. 6). A Canon EOS 60D DSLR camera with a Canon EF-S 1785 mm f/4–5.6 IS USM lens was used to record the motion of both filaments at 25 frames per second and resolution of 1920×1080 pixels per frame. The recorded data were processed by open source code [25].

Figure 7 presents the experimental (dashed lines) and theoretical (smooth lines) deflection patterns V_1 of filament 1 oscillating at frequency $\Omega = 0.5$ and amplitude at $\phi_1 = 15^\circ$ adjacent to filament 2. The inserts present the deflection of the free end of the filament $V_1(X = 1)$ for a full cycle

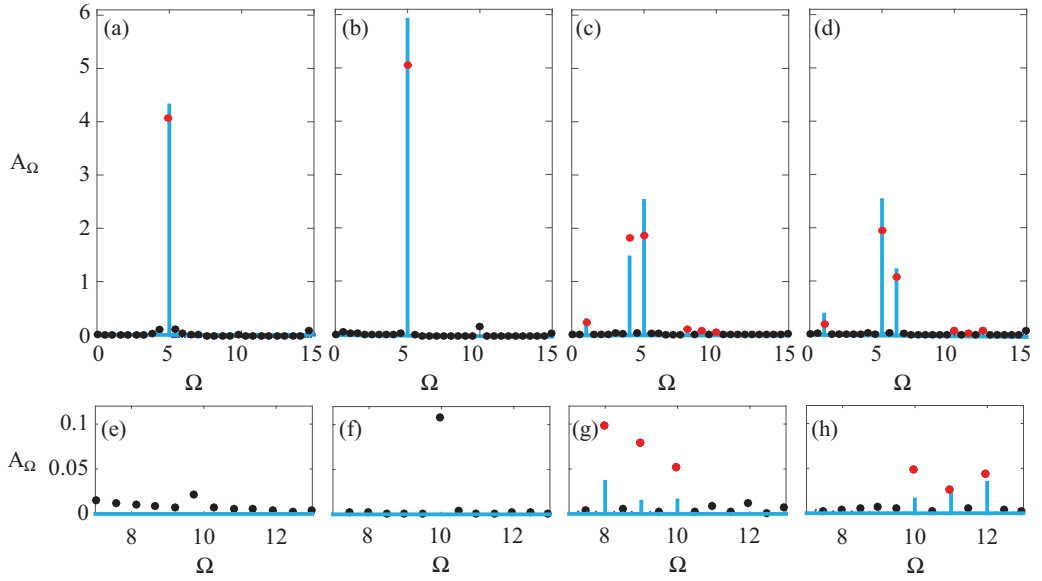

FIG. 8. Fourier decomposition of the experimental deflection V_1 at $X = 1$, presenting amplitude A_Ω vs frequency Ω. Panels (a)–(d) present the frequency decomposition of inserts of panels (a)–(d) in Fig. 7, respectively. Filled circle markers denote experimental data, and smooth blue lines denote the theoretical predictions. Red circles denote harmonics expected from the theoretical results. Panels (e)–(h) are magnifications of (a)–(d) in order to present the amplitudes of the $2\Omega_1$, $2\Omega_2$, and $\Omega_1 + \Omega_2$ first-order frequencies.

period defined as P. Dimensional values are related to the normalized values by $v_1 = V_1 \times 1.4\,\text{mm}$, $\omega = \Omega \times 0.1\,\text{Hz}$, $x = X \times 150\,\text{mm}$, and $t = T \times 0.62\,\text{s}$. For reference, panel (a) (movie 1 [26]) presents the deflection of an elastic filament oscillating without the presence of a second adjacent filament. Panel (b) (movie 2 [26]) presents the deflection V_1 for the case of an adjacent filament oscillating at identical frequency $\Omega_1 = \Omega_2$, identical amplitude $\phi_1 = \phi_2$, and without phase $\gamma = 0$. A significant increase in amplitude of the deflection is clearly evident, and the deflection patterns remain symmetric in this case. Panels (c) and (d) (movies 3 and 4 [26]) present the effect of an adjacent filament oscillating at a slightly smaller frequency ($\Omega_2 = 0.8\Omega_1$ in panel c) and a slightly higher frequency ($\Omega_2 = 1.2\Omega_1$ in panel d). Since $\Omega_1 \neq \Omega_2$ in panels (c) and (d), the interaction dynamics yields a slow mode with frequency of $(\Omega_1 - \Omega_2)$, which does not appear for cases in which $\Omega_1 = \Omega_2$. We choose to scale time so that the slow mode frequency is $\Omega_1 - \Omega_2 = 1$ and the total period is thus $P = 2\pi$, which is an integer multiplication of all other modes. The values of Ω_2 in panels (c) and (d) were chosen to be similar to Ω_1 in order to reduce the effective Sperm number of the $\Omega_1 - \Omega_2$ mode, thus increasing the first-order deflection to be experimentally significant.

Figure 8 presents frequency decomposition (based on MATLAB FFT function) of the experimental data presented in the inserts of Fig. 7. The blue smooth lines are the theoretical predictions, and the full circles are the experimental amplitudes (predicted frequencies are filled red circles and other frequencies are filled black circles). As expected, since $\Omega_1 \approx \Omega_2$ in panels (c), (d), the deflection is dominated by the frequencies of the actuation in leading-order Ω_1, Ω_2 and the $\Omega_1 - \Omega_2$ first-order harmonic. Panels (e)–(f) are magnifications of panels (a)–(d), focusing on of the amplitudes of the $2\Omega_1$, $2\Omega_1$, and $\Omega_1 + \Omega_2$ first-order frequencies. For all examined cases presented in Fig. 7, a good agreement (with errors $\approx 10\%$ or below) between the experimental data and the theoretical results is evident. Comparison of the amplitudes obtained from frequency decomposition, presented in Fig. 8, yields a reasonable agreement (with errors $\approx 20\%$ or below) for the leading order modes, (Ω_1, Ω_2). However, amplitude of higher-order modes presented in panels (c), (d), (g), (h) are small compared with the experimental resolution.

V. CONCLUDING REMARKS

This work examined analytically and experimentally the effect of hydrodynamic interaction between two adjacent waving elastic filaments on the forces and moments applied by the filaments. For similar actuation frequencies $\Omega_1 \approx \Omega_2$, the slowest $\Omega_1 - \Omega_2$ mode was shown to dominate the first-order dynamics since the amplitude of deflection is inverse to the effective Sperm number and the frequency of the mode. The time-averaged propulsion forces and moments are significantly affected from phase of the hydrodynamic interaction, which is an additional mechanism to break symmetry within the beating cycle. In addition, calculation of the effect of hydrodynamic interaction on the propulsive forces yielded that antiphase beating is optimal for time-averaged propulsion, in contrast with the commonly used assumption of maximal efficiency of the synchronized state. Calculation of turning moments due to phase difference yielded optimal maneuvering for phase of 90°.

The linearized elastic model and resistive-force theory applied in this work are limited by several geometric restrictions, such as small deflection to filament length and small changes of the gap between the filaments. While previous experimental studies such as Tony *et al.* [4] showed that the linearized model of a single filament [2] "appears to remain quantitatively correct well beyond its regime of strict validity," no such assurance exists for models involving hydrodynamic interaction, due to the additional requirement of small changes of the gap. Exception to this is in-phase actuation in which both filaments have identical deflection modes, and thus a nearly constant gap.

While the aim of the current work was the study of the effect of hydrodynamic interaction between adjacent filaments on artificial swimmers, the results may still provide insight for biological mechanisms which inherently involve elasticity. The presented analysis yielded that the effect of an adjacent oscillating filament, with identical in-phase actuation frequency and amplitude, is to decrease the effective Sperm number. Thus, the optimal propulsion oscillation frequency for an array of flagella may be expected to be greater compared with the optimal frequency of an isolated flagellum. Future work may examine nonlinear effects, internal actuation distributed along the filament, as well as a study of the dynamics of a lattice of oscillating filaments.

[1] K. E. Machin, Wave propagation along flagella, J. Exp. Biol. **35**, 796 (1958).
[2] C. H. Wiggins and R. E. Goldstein, Flexive and Propulsive Dynamics of Elastica at Low Reynolds Number, Phys. Rev. Lett. **80**, 3879 (1998).
[3] C. H. Wiggins, D. Riveline, A. Ott, and R. E. Goldstein, Trapping and wiggling: Elastohydrodynamics of driven microfilaments, Biophys. J. **74**, 1043 (1998).
[4] S. Y. Tony, E. Lauga, and A. E. Hosoi, Experimental investigations of elastic tail propulsion at low Reynolds number, Phys. Fluids **18**, 091701 (2006).
[5] S. Camalet and F. Jülicher, Generic aspects of axonemal beating, New J. Phys. **2**, 24 (2000).
[6] R. M. Arco, J. R. Vélez-Cordero, E. Lauga, and R. Zenit, Viscous pumping inspired by flexible propulsion, Bioinspir. Biomim. **9**, 036007 (2014).
[7] R. Golestanian, J. M. Yeomans, and N. Uchida, Hydrodynamic synchronization at low Reynolds number, Soft Matter **7**, 3074 (2011).
[8] E. Lauga and R. E. Goldstein, Dance of the microswimmers, Phys. Today **65**, 30 (2012).
[9] J. Gray, *Ciliary Movement* (Cambridge University Press, Cambridge, 2015).
[10] G. I. Taylor, Analysis of the swimming of microscopic organisms, Proc. R. Soc. London A **209**, 447 (1951).
[11] L. J. Fauci, Interaction of oscillating filaments: a computational study, J. Comput. Phys. **86**, 294 (1990).
[12] G. J. Elfring and E. Lauga, Passive hydrodynamic synchronization of two-dimensional swimming cells, Phys. Fluids **23**, 011902 (2011).
[13] G. J. Elfring and E. Lauga, Synchronization of flexible sheets, J. Fluid Mech. **674**, 163 (2011).
[14] C. Mettot and E. Lauga, Energetics of synchronized states in three-dimensional beating flagella, Phys. Rev. E **84**, 061905 (2011).

[15] D. R. Brumley, K. Y. Wan, M. Polin, and R. E. Goldstein, Flagellar synchronization through direct hydrodynamic interactions, Elife **3**, e02750 (2014).
[16] K. Y. Wan, K. C. Leptos, and R. E. Goldstein, Lag, lock, sync, slip: The many 'phases' of coupled flagella, J. R. Soc., Interface **11**, 20131160 (2014).
[17] D. M. Woolley, R. F. Crockett, W. D. I. Groom, and S. G. Revell, A study of synchronisation between the flagella of bull spermatozoa, with related observations, J. Exp. Biol. **212**, 2215 (2009).
[18] Y. Yang, J. Elgeti, and G. Gompper, Cooperation of sperm in two dimensions: Synchronization, attraction, and aggregation through hydrodynamic interactions, Phys. Rev. E **78**, 061903 (2008).
[19] Yi Man, L. Koens, and E. Lauga, Hydrodynamic interactions between nearby slender filaments, Europhys. Lett. **116**, 24002 (2016).
[20] R. E. Goldstein, E. Lauga, A. I. Pesci, and M. R. E. Proctor, Elastohydrodynamic synchronization of adjacent beating flagella, Phys. Rev. Fluids **1**, 073201 (2016).
[21] J. Gray and G. J. Hancock, The propulsion of sea-urchin spermatozoa, J. Exp. Biol. **32**, 802 (1955).
[22] J. Lighthill, *Mathematical Biofluiddynamics* (Society for Industrial and Applied Mathematics, Philadelphia, 1975).
[23] T. R. Powers, Role of body rotation in bacterial flagellar bundling, Phys. Rev. E **65**, 040903 (2002).
[24] B. M. Friedrich, I. H. Riedel-Kruse, J. Howard, and F. Jülicher, High-precision tracking of sperm swimming fine structure provides strong test of resistive force theory, J. Exp. Biol. **213**, 1226 (2010).
[25] T. L. Hedrick, Software techniques for two- and three-dimensional kinematic measurements of biological and biomimetic systems, Bioinspir. Biomim. **3**, 034001 (2008).
[26] See Supplemental Material at http://link.aps.org/supplemental/10.1103/PhysRevFluids.3.044203 for movies 1–4.